Available online at www.sciencedirect.com
SCIENCE DIRECT®
Corrosion Science 47 (2005) 735–755
CORROSION SCIENCE
www.elsevier.com/locate/corsci

Inhibitors performance in CO_2 corrosion EIS studies on the interaction between their molecular structure and steel microstructure

D.A. López *, S.N. Simison, S.R. de Sánchez

División Corrosión, INTEMA, Universidad Nacional de Mar del Plata, Av. Juan B. Justo 4302, B7608FDQ Mar del Plata, Argentina

Available online 14 August 2004

Abstract

The performance of three imidazoline-like inhibitors in CO_2 corrosion was studied by means of electrochemical measurements employing a.c. and d.c. techniques. Carbon steel with two different microstructures (annealed, and quenched and tempered (Q&T)) was used in a deoxygenated 5% wt. NaCl solution, saturated with CO_2 at 40 °C and pH 6. Aminopropylimidazol (API) and two commercial imidazoline-based products (PC and QB) were used as inhibitors. Electrochemical impedance spectroscopy (EIS) and linear polarization resistance (LRP) studies showed that the annealed samples have a better corrosion resistance than the Q&T samples when API and PC were added. On the other hand, the presence of QB yielded the opposite results. From the Bode phase angle plots it can be concluded that in the first case and for both microstructural conditions, there is no indication of formation of an inhibitor film, whereas in the presence of QB its formation is clearly evident. Based on these experimental findings, a mechanism of action for each inhibitor is proposed.

Keywords: Steel (A); EIS (B); Inhibition (C)

* Corresponding author. Tel.: +54 223 4816600x244; fax: +54 223 4810046.
E-mail address: dalopez@mdp.edu.ar (D.A. López).

0010-938X/$ - see front matter © 2004 Elsevier Ltd. All rights reserved.
doi:10.1016/j.corsci.2004.07.010

1. Introduction

Although the corrosion resistance of carbon steels to the environment in which they are used is limited, they are still widely used in the petroleum industry, mainly due to economical reasons. Usually these media contain high concentrations of chlorides and carbon dioxide. According to their chemical composition and their fabrication processes, these steels may have different microstructures which influence their mechanical properties and corrosion resistance.

As a consequence of corrosion processes, a layer of corrosion products is formed in the surface of the steel, and its protection properties depend on the environmental conditions and the characteristics of the material. The presence of iron carbonate ($FeCO_3$) is commonly related with the formation of protective layers [1]. Because of its low solubility (pK_{sp} = 10.54 at 25 °C [2]), $FeCO_3$ falls out of solution as a precipitate when ferrous cations (Fe^{2+}) interacts with carbonate (CO_3^{2-}) and bicarbonate (HCO_3^-) ions in the solution [3].

The surface scales formed below 40 °C in chloride media containing carbon dioxide consists mainly of cementite (Fe_3C) with some $FeCO_3$ and alloying elements of the steel [1,4]. Fe_3C is part of the original steel in the non-oxidized state that accumulates on the surface after the preferential dissolution of ferrite (α-Fe) into Fe^{2+}. It is suggested that cementite provides an available area for the cathodic reactions [5].

When the environment is highly aggressive or the scales formed on the steel are non-protective, the use of corrosion inhibitors is preferred. Inhibitors are chemical compounds added in small quantities in order to reduce the corrosion rate. Organic compounds containing nitrogen such as amines, amides, quaternary ammonium salts and specially imidazolines and their derivatives, are widely used in the petroleum industry with this purpose. They usually adsorb on the metallic surface generating a protective film that interferes with the electrochemical reactions involved in the corrosion processes. Despite their extensive use, their mechanism of action is mostly unknown.

The interaction between the molecular structure of the inhibitors and the influence of carbon steel microstructure in their performance is barely studied, even though its great importance in field applications. According to Rosenfeld et al. [6], inhibitors incorporate to the corrosion product layer and form a protective barrier between the base material and the corrosive media. French et al. [7] presented SEM results showing that the structure of the corrosion product layer is modified by the inhibitors. They suggested that the structure of the inhibitor must be the appropriate one to interact with the corrosion products and that they can be effective on iron carbonates or sulfides, but not effective on oxides. Oblonsky et al. [8] studied the adsorption of octadecyldimethylbenzylammonium chloride (ODBAC) to carbon steel with two different microstructures. They found that ODBAC physisorbs strongly to the ferritic–perlitic microstructure and weakly to the martensitic microstructure. They attributed the differences to the persistency of the passive films on the two microstructures, with the more stable passive film on the martensitic steel preventing optimal adsorption of the inhibitor.

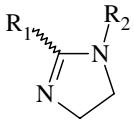

Fig. 1. Scheme of a typical imidazoline molecule.

The information regarding the molecular structure of imidazolines and their derivatives in relationship with their mechanisms of action in chloride media containing CO_2 is not conclusive. The molecular structure of imidazolines can be divided in three different substructures: a five-atom ring with nitrogen elements, a long hydrocarbon chain (R_1) and a pendant side chain with an active functional group (R_2) (Fig. 1). The functional groups in R_1 and R_2 can be variable. According to some authors [9–11], R_2 has a major influence in the performance of the compound, while for Edwards et al. [12] it has little effect on the imidazolines efficiency as corrosion inhibitors.

On the other hand, Jovancicevic et al. [13] studied the effect of R_1 by molecular modeling and concluded that the length of the hydrocarbon chain has a key role in the inhibitive behavior of the imidazolines. Nevertheless, other authors [11,14] consider that the length of this chain is not a critical factor regarding the inhibitory properties of the compound. Due to the widespread usage of imidazoline derivatives as inhibitors in the petroleum industry and the lack of a general explanation for the influence of steel microstructure on inhibitor performance in CO_2 corrosion, it is important to have a better understanding of the inhibition mechanism considering both the molecular structure of these compounds and the microstructural steel properties.

EIS has proved to be a powerful technique to study corrosion processes and inhibitor performance in different environments [15–17]. In the present work, both EIS and some standard d.c. measurements (LRP, E_{corr}) were employed to study the performance of three imidazoline-based inhibitors in carbon steel with two different microstructures (annealed and Q&T) in CO_2 saturated media with a high content of chlorides.

2. Experimental

Carbon steel with composition (% wt.) 0.99Mn–0.38C–0.33Si–0.17Cr–0.09Cu–0.04Ni–0.02Mo–<0.01P–<0.01S–Fe balance was used. Two different heat treatments were performed on the samples: annealing; austenized at 890 °C and furnace cooled (sample H); and quenching and tempering; austenized at 890 °C, water Q&T 1 h at 700 °C (sample T). Fig. 2 shows the microstructures of both samples under study.

Working electrodes were machined from these heat-treated materials into 5 mm diameter bars, cut and mounted with epoxy resin in a disc electrode holder. Electrical contact between sample and holder was made with silver loaded epoxy resin.

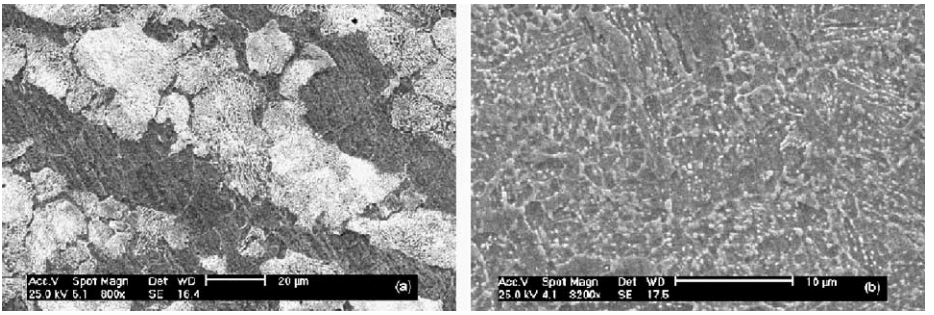

Fig. 2. Microstructure of the carbon steels specimens (Nital etched): (a) samples H and (b) samples T.

Surfaces were polished with 600-grit SiC paper for electrochemical studies and with 0.05 μm alumina until mirror finish for microstructure characterization. In the last case the samples were etched with Nital and observed with scanning electron microscope (SEM Phillips XL 30).

Experiments were conducted at atmospheric pressure, 40 °C and with low speed stirring (100 rpm) to ensure laminar flow conditions. Three-electrode jacketed test cells were used with a concentric Pt ring as counter electrode. A saturated calomel electrode was chosen as reference. Test solution was 5% wt. aqueous NaCl (analytical-reagent grade), saturated with deoxygenated CO_2 and a working volume of 0.5 l. A set of glass columns containing silica gel and CrO_3 treated with hot O_2, N_2 and CO was employed as an oxygen scavenger to remove impurities from commercial CO_2 (99.98%). The oxygen concentration of the solution was measured with a DCR OXI200 (Chemetrics®) and was kept below 40 ppb during the experiments. A positive pressure of deoxygenated CO_2 was maintained in the cells during the experiments minimizing the possibility of air ingress. Chemetrics® colorimetric ampoules were used to measure the dissolved CO_2 concentration as H_2CO_3 and the values were 1000 ppm in all the tests. Fifteen milliliters of deoxygenated 1.0 M aq. $NaHCO_3$ were added to adjust the pH to 6. The samples were immersed in the working solution and evaluated during 96 h. Aminopropylimidazol (API, analytical-reagent grade 98%; $R_1 = H$, $R_2 = (CH_2)_3–NH_2$) and two commercial imidazoline-based products (PC: $R_1 = (CH_2)_n–N^+H_3$ $n = 8–12$, $R_2 = (CH_2)_2–NH_2$; and QB: $R_1 = (CH_2)_n–CH_3$ $n = 10–17$, $R_2 = (CH_2)_2–NH_2$) were used as inhibitors. The API concentration in the test solution was 100 ppm. Specifications from the manufacturers were considered for the commercial products, using concentrations of 20 ppm for PC and 50 ppm for QB during the tests.

A Solartron 1280B unit was used for the electrochemical measurements. EIS was measured at the corrosion potential (E_{corr}) using an applied potential of ± 0.005 V rms and a frequency range of 20,000–0.05 Hz. Linear polarization resistance (LRP) was measured by polarizing the working electrode ± 0.015 V vs. E_{corr} with a sweep rate of 10^{-4} V/s. The corrosion potential was also monitored before and after d.c. and a.c. analyses. Measurements were taken at 2, 24, 48, 72 and 96 h after exposure.

The efficiency of inhibition (η) was calculated by

$$\eta(\%) = [(R_{ct,i} - R_{ct,b})/R_{ct,i}] \times 100 \quad (1)$$

where, $R_{ct,i}$ is the charge transfer resistance in test with inhibitor; $R_{ct,b}$ is the charge transfer resistance in test without inhibitor.

3. Results and discussion

3.1. Aminopropylimidazol (API, 100 ppm)

The impedance diagrams for samples H and samples T obtained after 2, 24, 48, 72 and 96 h of immersion with API are presented in the Nyquist plots in Fig. 3. The magnitude of the impedance increases continuously with time for samples H whereas for samples T the values stabilize after 48 h of exposure. All experimental plots have a depressed semicircular shape in the complex impedance plane, with the center under the real axis, which is a typical behavior for solid metal electrodes that show frequency dispersion of the impedance data [18]. The efficiency calculated by Eq. (1) at 96 h of immersion time for samples H is 6.2% and for samples T is −22.6%. Thus, API has a protective effect in the annealed samples and an activation effect for the Q&T ones.

Fig. 4 presents the impedance diagrams for the same experimental data in the Bode format $\log f$ vs. θ for both microstructural conditions. A sole time constant can be observed and a maximum phase angle increasing with time and shifting to lower frequencies. The later is usually correlated with a growth of the system capacitance at longer immersion times [19].

Fig. 5 shows the electrical equivalent circuit employed to analyze the impedance plots. In order to take into account the non-ideal frequency response of the displayed data, a constant phase element (CPE) was used instead of an ideal capacitor. The impedance of a CPE is described by the expression:

$$Z_{CPE} = Y^{-1}(i\omega)^{-n} \quad (2)$$

where Y is a proportional factor, 'i' is $\sqrt{-1}$, ω is $2\pi f$ and n has the meaning of a phase shift [18]. From the equivalent circuit, R_s is the electrolyte resistance (Ωcm^2), R_{ct} is the charge transfer resistance (Ωcm^2) and Y ($\Omega^{-1} cm^{-2} s^n$) and n are the parameters depicted for Z_{CPE} in Eq. (2). Excellent fit with the model was obtained for all experimental data. As an example, the Nyquist and Bode plots at 72 h for samples H are presented in Fig. 6a and b, respectively. The fitted data follows almost the same pattern as the experimental results along the whole diagrams, with an average error of about 3% in all cases. The fitted parameters for both microstructural conditions are shown in Tables 1 and 2.

Fig. 7 shows the main parameters obtained with d.c. and a.c. measurements for both microstructures with 100 ppm of API. It was observed that, in despite of slight differences, both R_p and R_{ct} follow the same pattern. It is also worth noting that the

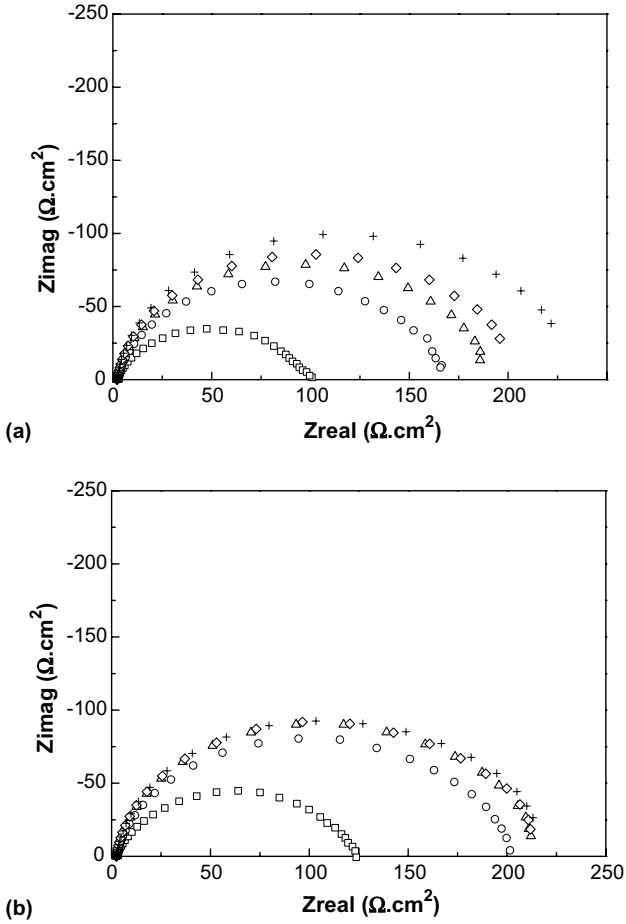

Fig. 3. EIS Nyquist plots at different times of immersion with API:
(a) samples H, (b) samples T; (□) 2 h, (○) 24 h, (△) 48 h, (◇) 72 h, (+) 96 h.

E_{corr} values are not influenced by the heat treatment and show a small drift in the anodic direction at longer times of exposure.

The fitting results show that the proportional factor Y of CPE increases with time without significant differences in the values obtained at each time for both microstructural conditions. As proposed in a previous work [15], this increase in the capacitance (Y) could be related to the growing area of an iron carbonate deposit on the surface of the samples. At 40 °C these scales are porous and inhomogeneous allowing the access of the corroding solution to the base material. These scales, however, seem to provide some corrosion protection to the metal beneath them by restricting the mass transfer of reactants and products between the bulk solution and the metal, which is represented by an increase in the corresponding R_{ct} values. On the other

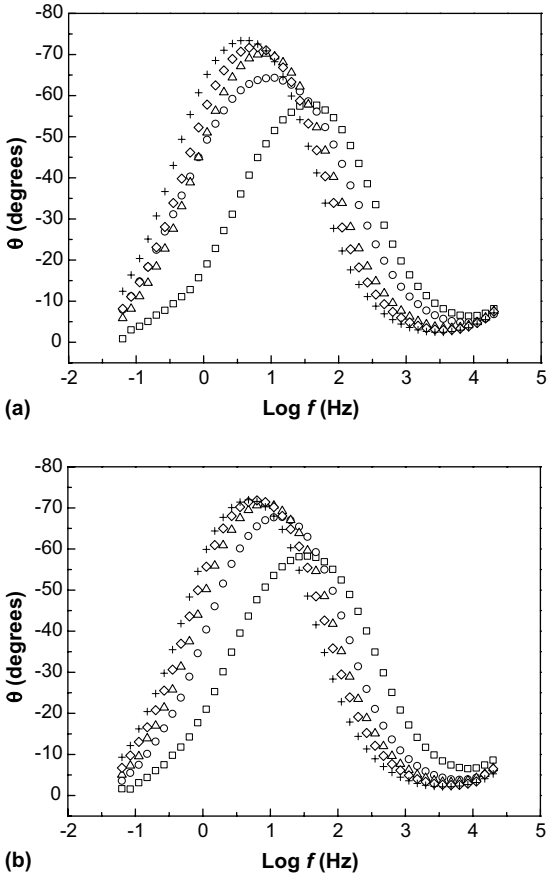

Fig. 4. EIS Bode log$f$ vs. θ plots at different times of immersion with API: (a) samples H, (b) samples T; (□) 2 h, (○) 24 h, (△) 48 h, (◇) 72 h, (+) 96 h.

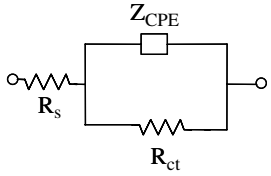

Fig. 5. Equivalent circuit used to represent the impedance results.

hand, there is no evidence of the formation of a protective $FeCO_3$ film because there is just one capacitive arch in the EIS Nyquist plots and a single time constant in the EIS Bode plots [20]. This could be due to the formation of a porous thin layer of $FeCO_3$ with a resistance that is much smaller than the charge transfer resistance

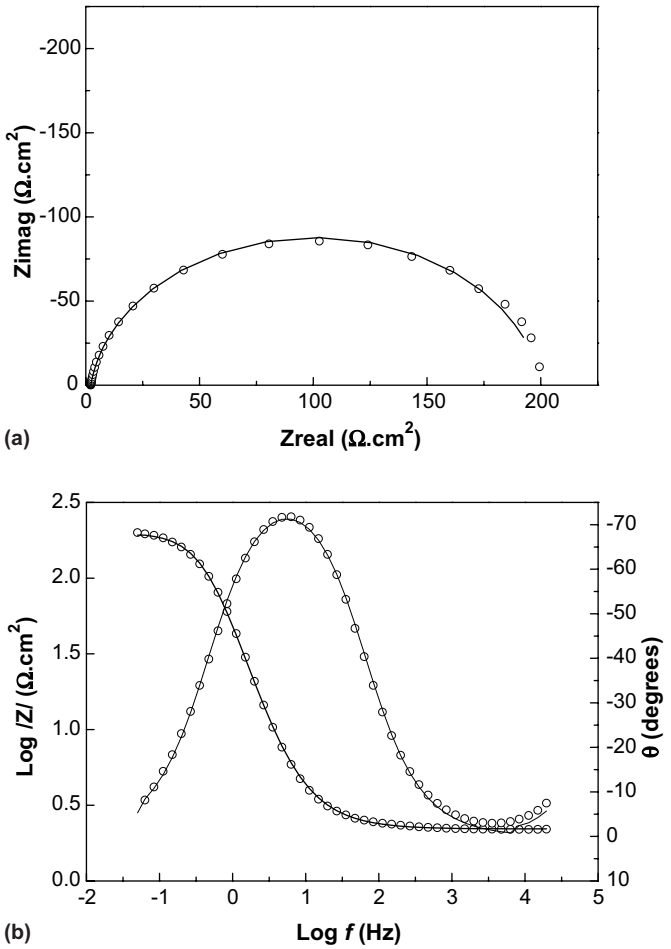

Fig. 6. EIS Nyquist (a) and Bode (b) plots at 72 h for samples H with API: (O) experimental data, (—) fitting model.

Table 1
Circuit parameters for samples H with API

Time (h)	R_s (Ωcm^2)	R_{ct} (Ωcm^2)	Y ($\Omega^{-1} cm^{-2} s^n \times 10^4$)	n
2	2.3	95	8.77	0.82
24	2.2	164	11.25	0.88
48	2.2	186	14.93	0.91
72	2.2	198	18.15	0.92
96	2.2	225	22.74	0.93

(R_{ct}). The semicircle representing the $FeCO_3$ film merges with the charge transfer loop and hence the EIS data are described by a simple capacitive semicircle [21].

Table 2
Circuit parameters for samples T with API

Time (h)	R_s (Ωcm^2)	R_{ct} (Ωcm^2)	Y ($\Omega^{-1} cm^{-2} s^n \times 10^4$)	n
2	2.5	121	8.05	0.81
24	2.5	196	9.63	0.89
48	2.5	210	12.09	0.92
72	2.4	210	15.00	0.93
96	2.7	212	18.04	0.94

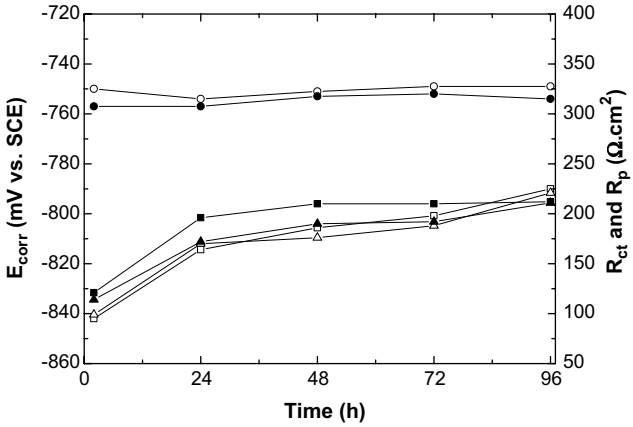

Fig. 7. E_{corr}, R_{ct} and R_p for both microstructures with API: (○) E_{corr}, (□) R_{ct}, (△) R_p; (open symbols) samples H, (filled symbols) samples T.

The protective action of the azole compounds can be explained taking into account the interaction that takes place between the inhibitor molecules and the metallic substrate. The pyridine-like (sp^2) nitrogen atom in the imidazolines would act as a Lewis base [22], while Fe^{3+}, Fe^{2+} and metallic Fe would behave like acids, acting as electron acceptors, with higher acidity corresponding to higher oxidation state. Thus, the interaction with the inhibitor would proceed mainly due to the presence of long-range electrostatic forces [22]. In our particular case, the higher Lewis acidity of Fe_3C compared to metallic iron (α-Fe) sites present in the samples, provides a preferential site on the surface for the interaction with the inhibitor [23]. This way, the inhibitor can act by blockaging the active sites or generating a sort of physical barrier to reduce the transport of corrosive species to the metal surface.

According to authors [12–14], the presence of long hydrocarbon chains as R_1 in the structure of the imidazolines is responsible of their capacity of forming protective barriers against aggressive ions from the bulk solution. The lack of such chains in the API structure could be related to the absence of this kind of barrier, as shown by the impedance plots.

Table 3
Circuit parameters for samples H without inhibitor

Time (h)	R_s (Ωcm^2)	R_{ct} (Ωcm^2)	Y ($\Omega^{-1} cm^{-2} s^n \times 10^4$)	n
2	2.1	123	6.98	0.83
24	2.9	176	11.96	0.90
48	3.1	192	18.52	0.91
72	2.8	210	24.09	0.91
96	2.2	211	30.10	0.92

Table 4
Circuit parameters for samples T without inhibitor

Time (h)	R_s (Ωcm^2)	R_{ct} (Ωcm^2)	Y ($\Omega^{-1} cm^{-2} s^n \times 10^4$)	n
2	2.0	137	7.17	0.83
24	3.2	182	11.27	0.90
48	2.3	205	17.65	0.91
72	2.0	257	21.13	0.92
96	1.8	260	31.03	0.93

In order to allow the comparison of the results obtained with and without inhibitors addition, Tables 3 and 4 presents the fitted parameters for the later condition [15]. It can be seen that the capacitance (Y) for the samples treated with API show lower values compared to those obtained without inhibitor. Thus, the presence of the inhibitor could be somehow interfering with the formation of $FeCO_3$. Therefore, API can only act by blocking the cathodic sites at Fe_3C, generating a retarding effect in the formation of $FeCO_3$.

The differences observed between both microstructural conditions can be explained by taking into account the characteristics of the corrosion process for each kind of sample [15]. When the annealed samples are exposed to the corrosive fluid, the corrosion process yields an increase in the area of Fe_3C exposed. That is because the dissolution of the surrounding ferrite (α-Fe) from pearlite leaves a laminar structure of non-oxidized Fe_3C, which is not removed from the sample surface. Then, API interacts with the laminar Fe_3C and the adsorbed molecules block the active site for further cathodic reactions. The final result averaging this obstruction process and the slower formation of $FeCO_3$ yields a favorable relation with an increase of R_{ct}. The low efficiency acquired (6.2%), can then be related to the incapability of the inhibitor to form a protective barrier.

In the case of the Q&T samples, the inhibitor interacts with the globular Fe_3C generating the same blocking and retarding effect as in the annealed samples. But unlike samples H, as the corrosion process takes place, the carbides detach from the metal and are removed from the sample surface. The corrosion process continues and a new area of uncovered cementite appears at the surface. Therefore, in the Q&T samples the inhibitor would only produce a delay in the $FeCO_3$ precipitation and does not provide any appreciable protection due to cathodic blocking. This would

explain the negative efficiency or activation process calculated for this microstructural condition.

3.2. Commercial inhibitor I (PC, 20 ppm)

The impedance diagrams obtained at various immersion times for samples H and T with inhibitor PC are presented as Nyquist plots in Fig. 8. The magnitude of the impedance increases with time up to 72 h for samples H while for samples T the impedance values stabilize after 48 h of exposure reaching similar values as the annealed samples at that time. All experimental plots have a depressed semicircular shape in the complex impedance plane, with the center under the real axis. The efficiency after 96 h of immersion time for samples H is 72.4% and for samples T is 39.8%.

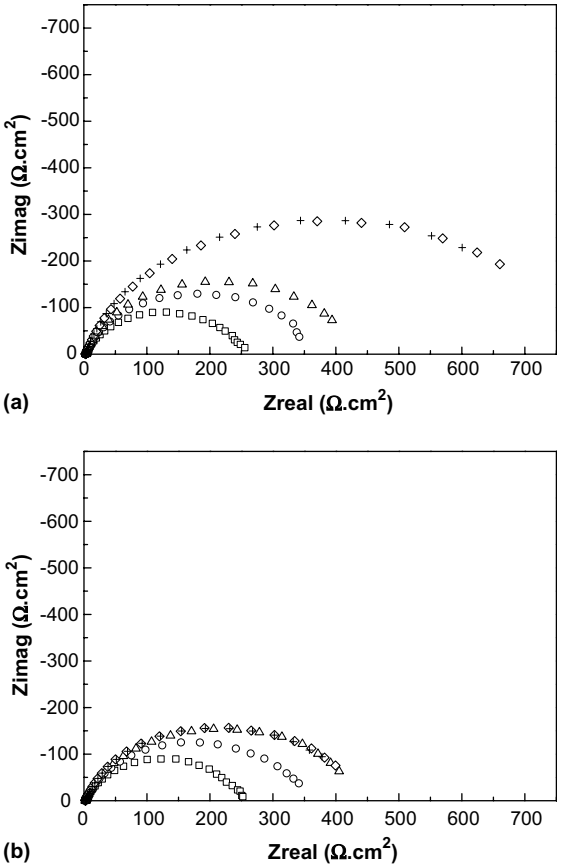

Fig. 8. EIS Nyquist plots at different times of immersion with PC:
(a) samples H, (b) samples T; (□) 2 h, (○) 24 h, (△) 48 h, (◇) 72 h, (+) 96 h.

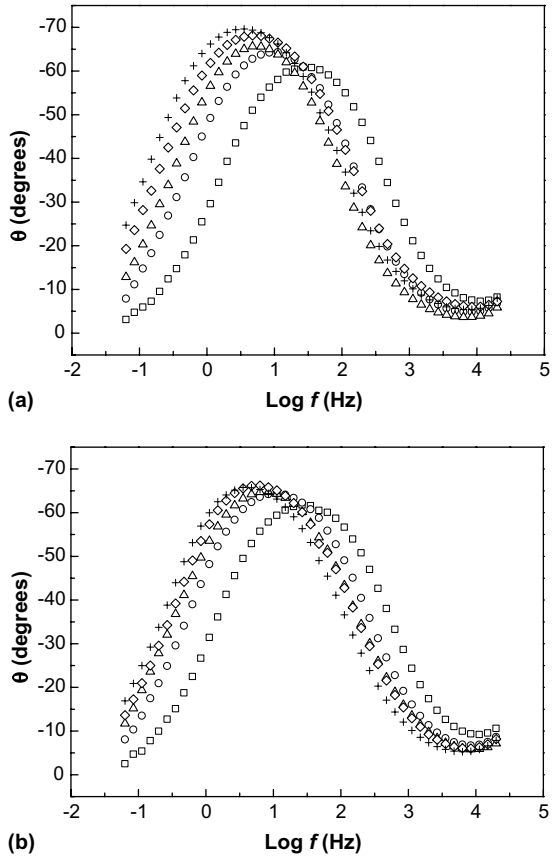

Fig. 9. EIS Bode log$f$ vs. θ plots at different times of immersion with PC: (a) samples H, (b) samples T; (□) 2 h, (○) 24 h, (△) 48 h, (◊) 72 h, (+) 96 h.

The impedance diagrams for the same experimental data in the Bode format log$f$ vs. θ for both microstructural conditions are presented in Fig. 9. As in the case with API, a sole time constant is present and the maximum phase angle increases with time and shifts to lower frequencies. Consequently, the same electrical equivalent circuit was employed to analyze the impedance plots (Fig. 5) with optimal correlation (figure not shown). The corresponding fitted parameters are shown in Tables 5 and 6.

Fig. 10 presents the evolution of R_p, R_{ct} and E_{corr} in time for both microstructures with PC. It can be seen that both R_p and R_{ct} follow the same pattern and that the inhibitor addition does not cause any shift in the corrosion potential.

Similarly to the case in which API was added, the capacitance (Y) increases with time although there are no evidences of a film formation due to a protective $FeCO_3$ deposit or a protective inhibitor layer. However, tests performed by surface analysis techniques showed a partial stabilization of $FeCO_3$ in the samples surface, particularly in the annealed ones [24]. As seen with API, capacitance values are lower when

Table 5
Circuit parameters for samples H with PC

Time (h)	R_s (Ωcm^2)	R_{ct} (Ωcm^2)	Y ($\Omega^{-1} cm^{-2} s^n \times 10^4$)	n
2	2.7	252	6.47	0.80
24	2.9	355	11.41	0.82
48	3.5	417	13.88	0.83
72	2.9	776	11.60	0.82
96	2.5	764	16.05	0.83

Table 6
Circuit parameters for samples T with PC

Time (h)	R_s (Ωcm^2)	R_{ct} (Ωcm^2)	Y ($\Omega^{-1} cm^{-2} s^n \times 10^4$)	n
2	2.1	251	7.14	0.80
24	2.2	349	11.41	0.81
48	2.5	434	13.24	0.80
72	2.2	435	14.78	0.81
96	2.5	432	18.53	0.81

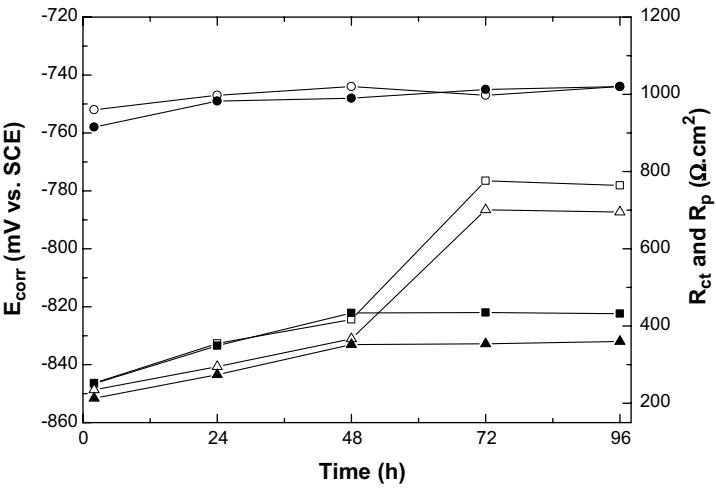

Fig. 10. E_{corr}, R_{ct} and R_p for both microstructures with PC: (○) E_{corr}, (□) R_{ct}, (△) R_p; (open symbols) samples H, (filled symbols) samples T.

PC is present compared to the situation without inhibitor. This could be explained considering the formation of a thicker $FeCO_3$ deposit onto a similar area than that of the uninhibited samples.

In contrast with the inhibitor previously studied, PC has a hydrocarbon chain (R_1) that could generate stabilizing interactions among the PC molecules constructing a barrier to the aggressive ions from the solution bulk. Nevertheless, the terminal

ammonium group in the chain could also have repulsive effects due to the positive charge, resulting in an inhomogeneous and porous lattice. Thus, the adsorption of PC on cementite sites by acid–base interactions could lead to the blockage of the active sites and at the same time, the formation of occlusion cells or stagnant areas due to the interaction among the R_1 tails. In such areas, the dissolved ferrite could result into a localized concentration of Fe^{2+}. Due to the hydrophilic nature of the net generated, ions such as carbonates and bicarbonates could migrate into these cells and form $FeCO_3$. This process is favored in samples H because of the laminar structure of the Fe_3C, which provides better anchoring sites [25].

Once again, the differences observed in the efficiency values for each microstructural condition can be explained taking into account the corrosion process that occurs in every case. As a consequence of the absence of a protective film the corrosion process continues in time for both kind of samples. For the annealed samples, the inhibitor has the double effect of blocking active sites in Fe_3C areas and, at the same time, generating occlusion cells as mentioned above, where the formation of $FeCO_3$ is favored. An increase in the ratio Fe_3C/α-Fe as the corrosion process continues results in a major accumulation of species amid the cementite platelets.

For the Q&T samples a similar situation is observed, but as the corrosion process continues, the globular Fe_3C detaches from the metal and is removed from the sample surface. Therefore, the protective effect of the inhibitor is diminished compared to that in the annealed samples.

Finally, the ability to produce more $FeCO_3$ due to the interaction of the inhibitor with the surface, yields lower corrosion rates for the samples treated with PC compared to those with API, although the efficiency observed is also higher for samples H in relation with samples T.

3.3. Commercial inhibitor II (QB, 50 ppm)

The impedance diagrams for samples H and samples T obtained after 2, 24, 48, 72 and 96 h of immersion with inhibitor QB are presented in the Nyquist plots in Fig. 11. In both cases the magnitude of the impedance increases greatly after 24 h and reaches values considerably higher compared to those observed with the addition of PC. The efficiency at 96 h of immersion time for samples H is 97.4% and for samples T is 97.9%. However, the R_{ct} values obtained in samples T are about a 50% higher than those from samples H, indicating lower corrosion rates for the Q&T material.

Fig. 12 presents the impedance diagrams for the same experimental data in the Bode format $\log f$ vs. θ. Contrary to the situation observed with the other inhibitors, the Bode diagrams clearly shown the presence of two distinct time constants. This new time constant at higher frequencies could be related with the formation of a surface film in the samples due to the inhibitor presence [17]. Thus, a more complex electrical equivalent circuit was needed to analyze the impedance plots (Fig. 13). Here, R_s represents the electrolyte resistance, Z_{CPEf} is related to the non-ideal capacitance of the inhibitor film, R_{po} is related to the resistance of the film, Z_{CPEdl} is related to the non-ideal capacitance of the double layer of the bare metal and R_{dl} is the charge transfer resistance. Optimum fit with the model was obtained for all experimental

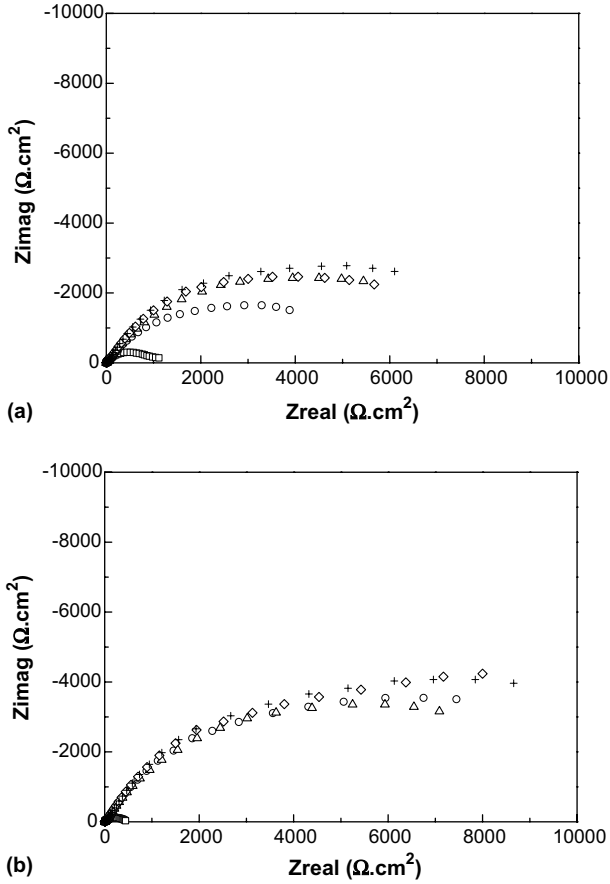

Fig. 11. EIS Nyquist plots at different times of immersion with QB: (a) samples H, (b) samples T; (□) 2 h, (○) 24 h, (△) 48 h, (◊) 72 h, (+) 96 h.

data. As an example, the Nyquist and Bode plots at 48 h for samples H are presented in Fig. 14a and b, respectively. The fitted data clearly follows pattern of the experimental results along the entire diagram, with an average error of about 3% in all cases. The corresponding fitted parameters are shown in Tables 7 and 8.

Fig. 15 shows the main parameters obtained with d.c. and a.c. measurements for both microstructures with 50 ppm of QB. It can be seen that both R_p and R_{ct} ($R_{po} + R_{dl}$) show the same pattern and that the final values of polarization resistance are clearly differenced for each microstructural condition. On the other hand, both kind of samples present an anodic shift in the E_{corr}, which is characteristic of anodic and anodic/cathodic inhibitors that form a protective film [13]. The presence of such a protective surface film is supported by the data acquired by surface analysis techniques [24].

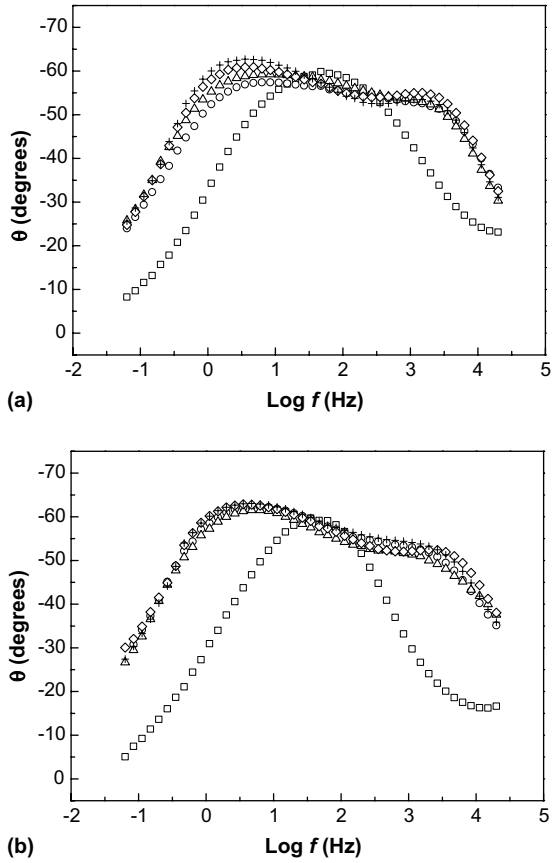

Fig. 12. EIS Bode log f vs. θ plots at different times of immersion with QB: (a) samples H, (b) samples T; (□) 2 h, (○) 24 h, (△) 48 h, (◇) 72 h, (+) 96 h.

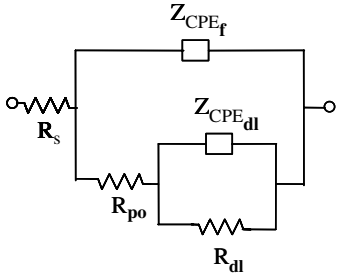

Fig. 13. Equivalent circuit used to represent the impedance results with film formation.

From the fitted parameters it can be seen that the capacitance values Y_{dl} reach a steady value after the surface film is formed. This is accompanied by the stabilization

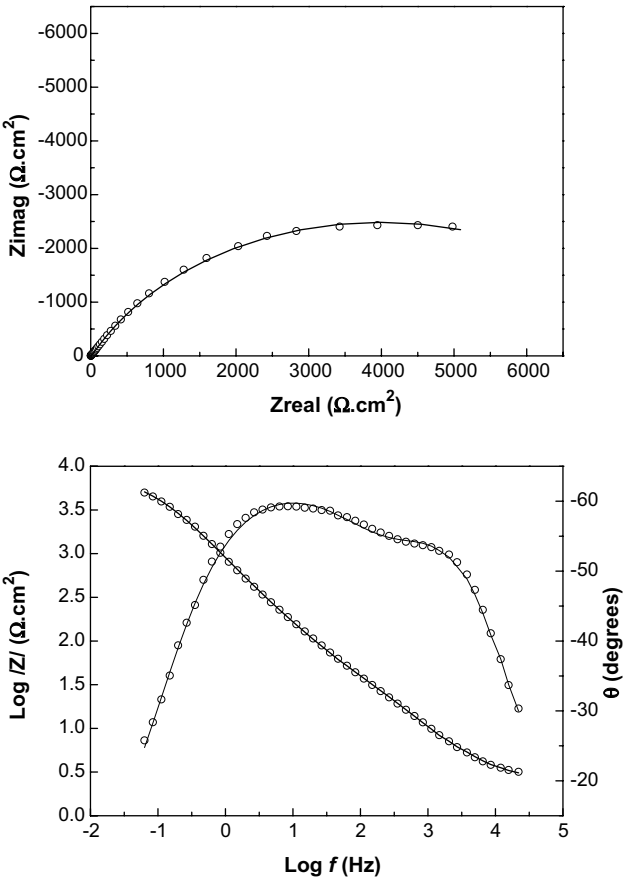

Fig. 14. EIS Nyquist (a) and Bode (b) plots at 48 h for samples H with QB: (O) experimental data, (—) fitting model.

Table 7
Circuit parameters for samples H with QB

Time (h)	R_s (Ωcm^2)	R_{po} (Ωcm^2)	$Y_f \times 10^4$ ($\Omega^{-1} cm^{-2} s^n$)	n_f	R_{dl} (Ωcm^2)	$Y_{dl} \times 10^4$ ($\Omega^{-1} cm^{-2} s^n$)	n_{dl}
2	2.9	–	–	–	1049	3.20	0.70
24	2.0	49	0.66	0.77	5537	1.50	0.65
48	2.3	91	0.82	0.74	7891	0.81	0.68
72	2.2	93	0.61	0.77	7674	0.88	0.72
96	2.1	94	0.77	0.75	8253	0.69	0.77

of the R_{dl} values, which occurs after 48 h for samples H and after 24 h for samples T. On the other hand, the R_{po} values present a similar behavior with higher values for

Table 8
Circuit parameters for samples T with QB

Time (h)	R_s (Ωcm^2)	R_{po} (Ωcm^2)	$Y_f \times 10^4$ ($\Omega^{-1} cm^{-2} s^n$)	n_f	R_{dl} (Ωcm^2)	$Y_{dl} \times 10^4$ ($\Omega^{-1} cm^{-2} s^n$)	n_{dl}
2	2.7	–	–	–	414	5.88	0.74
24	2.3	127	0.91	0.72	10,561	0.40	0.77
48	2.4	125	0.77	0.71	10,140	0.48	0.78
72	1.6	117	0.90	0.71	12,238	0.35	0.80
96	2.3	130	0.73	0.74	12,171	0.41	0.77

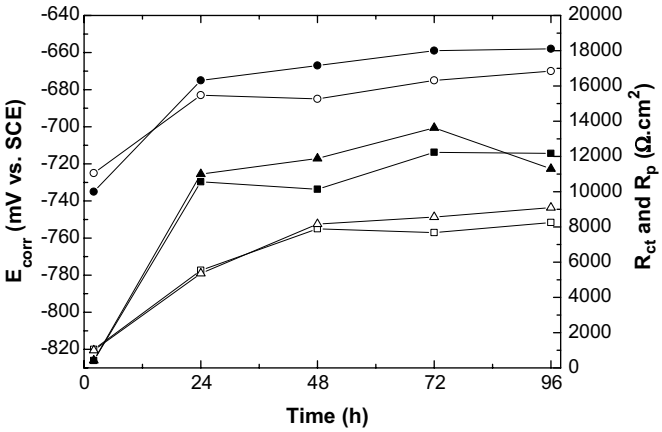

Fig. 15. E_{corr}, R_{ct} and R_p for both microstructures with QB: (○) E_{corr}, (□) R_{ct}, (△) R_p; (open symbols) samples H, (filled symbols) samples T.

samples T. Finally, the capacitance values associated with the surface film, Y_f, are similar for both microstructural conditions.

Fig. 12 shows that in the region of lower frequencies the phase angle reduces gradually, retiring from the value of 90° which corresponds to a pure capacitive behavior. This is an evidence of the presence of a porous film, where R_{po} would be related to the resistance of these pores to the passage of the electrolyte [19].

The higher values of R_{po} observed for samples T could be associated with a smaller pore size and, correspondingly, with the formation of a more compact film [19]. As a result, there is higher resistance to corrosion and higher values of R_{dl} are measured, compared to those of samples H.

The experimental results clearly show that a protective film is formed when the samples are treated with QB. This film reduces drastically the corrosion process in such a way that globular carbides are no longer detached from the surface in samples T.

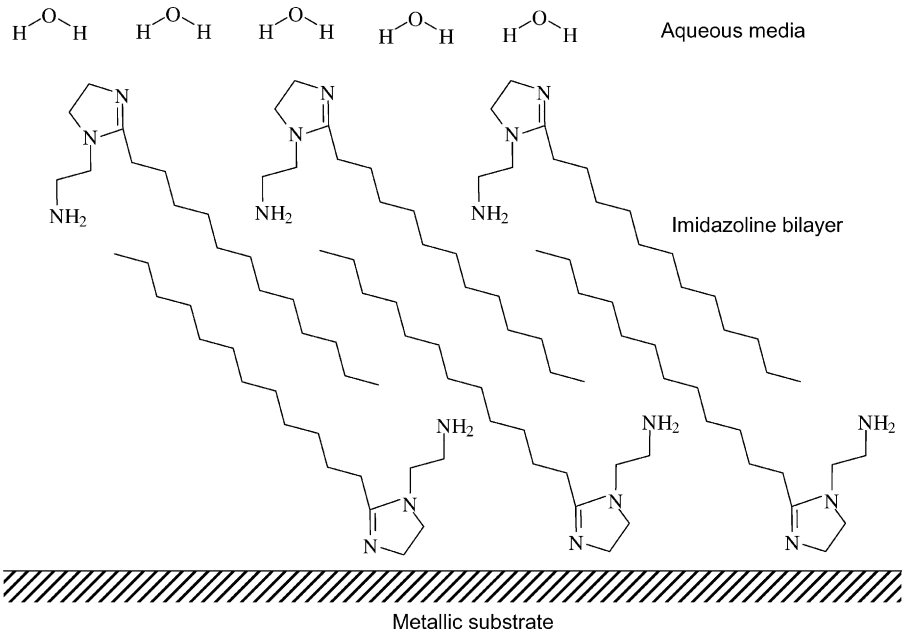

Fig. 16. Bilayer schematic model for QB inhibitor.

In contrast to the other inhibitors studied, QB has a long hydrocarbon chain R_1 with hydrophobic properties. The interactions among these chains can lead to the formation of a structure or molecular array, of which the most thermodynamically stable is a bilayer model (Fig. 16) [13]. A high hydration level on the samples surface, as determined by XPS analyses [24], seems to confirm this hypothesis.

To explain the differences achieved in the corrosion resistance for each microstructural condition it is necessary to take into account the morphological feature at the beginning of the corrosion tests (Fig. 2). Considering that the inhibitor will interact with the exposed Fe_3C through Lewis acid–base interactions, the morphology and distribution of these iron carbides are essential factors to take into account. In the annealed samples, the ferritic–perlitic microstructure has well defined areas of α-Fe and pearlite due to the lamination process during the fabrication of the material. Thus, the inhibitor could act rapidly in the pearlite areas, but the increase in the protective effect would be progressive according to the appearance of new areas of cementite revealed after the corrosion of the α-Fe areas. The characteristic surface irregularities of these samples would lead to a protective film, but with bigger pore size, as shown by the impedance results.

On the other hand, the quenched and tempered samples present a surface that has a homogeneous distribution of the globular iron carbides. Consequently, QB molecules can distribute uniformly on the samples, yielding a more compact film (higher R_{po}) in shorter time, with lower corrosion rates (higher R_{dl}).

4. Conclusions

Electrochemical impedance spectroscopy has been shown to be a useful tool for studying the corrosion process in the presence of CO_2 and evaluating the mechanism of action of three imidazoline derivatives as corrosion inhibitors.

When 100 ppm of API inhibitor and 20 ppm of PC inhibitor are used, the annealed samples present a better efficiency compared to the Q&T ones. In these cases no protective film formed and the corrosion process continued through time. Due to the globular morphology of the iron carbides in samples T, as the α-Fe is corroded these carbides are detached and removed from the surface of the samples. Thus, the blocking effect of active sites by the inhibitor is drastically diminished respect to the case observed in samples H, where iron carbides have a laminar structure. This effect is more pronounced when API is employed, having an activation effect on the corrosion rate for samples T.

The presence of 50 ppm of QB produces the formation of a protective film that reduces drastically the corrosion process. Despite both microstructural conditions present efficiencies of nearly 100%, the performance of samples T is about 50% superior to samples H. The different morphology and distribution of Fe_3C in each sample could be related with the protective qualities of the film formed on the samples.

The molecular structure of the compounds employed as inhibitors has a main role in their performance in the experimental conditions studied. From the data obtained it can be concluded that API is not a particularly useful inhibitor. The absence of a hydrocarbon chain R_1 seems to correlate to its incapability to form a protective layer.

The use of PC improves the efficiency observed for both microstructural conditions. The existence of a hydrocarbon chain R_1 with hydrophilic properties seems to impede the formation of a protective film, although it could be able to generate occlusion cells where the formation of a somewhat protective $FeCO_3$ is favored.

The best results in corrosion inhibition are found when QB is used as inhibitor. The presence of a long hydrocarbon chain R_1 with hydrophobic properties could be associated with the formation of a protective, yet porous film, that reduces drastically the corrosion process. A bilayer model seems to be the more appropriate array for the film structure.

From these results, it was demonstrated that not only the molecular structure of the inhibitor molecule is important when determining its performance in chlorine media containing deoxygenated CO_2, but also the microstructure of the steel to be used as working material.

Acknowledgements

This work was supported by the Argentine Research Council for Science and Technology (CONICET, grant PIP 0413/98), TWAS (grant 01-216/7 RG/CHE/LA) and the University of Mar del Plata. Test materials were provided by CINI, FUDETEC.

One of the authors (D.A.L.) is grateful to Dr. Silvia Ceré and Dr. Omar López for their valuable assistance and helpful comments during the revision of this paper.

References

[1] K. Videm, A. Dugstad, MP 28 (3) (1989) 63.
[2] D.R. Lide (Ed.), Handbook of Chemistry and Physics, 79th ed., CRC Press, Boca Raton, FL, 1998–1999.
[3] J.K. Heuer, J.F. Stubbings, Corros. Sci. 41 (7) (1999) 1231.
[4] D.A. López, W.H. Schreiner, S.R. de Sánchez, S.N. Simison, Appl. Surf. Sci. 207 (2003) 69.
[5] J.L. Mora-Mendoza, S. Turgoose, Corros. Sci. 44 (6) (2002) 1223.
[6] I.L. Rosenfeld, D.B. Bogomolov, A.E. Gorodetskii, L.P. Kazanskii, L.V. Frolova, L.I. Shamova, Z. Metallakd. 18 (2) (1982) 163.
[7] E.C. French, R.L. Martin, J.A. Dougherty, MP 28 (8) (1989) 46.
[8] L.J. Oblonsky, G.R. Chesnut, T.M. Devine, Corrosion 51 (1995) 891.
[9] X. Zhang, F. Wang, Y. He, Y. Du, Corros. Sci. 43 (8) (2001) 1417.
[10] D. Wang, S. Yong, M. Wang, H. Xiao, Z. Chen, Corros. Sci. 41 (10) (1999) 1911.
[11] J. Cruz, L.M.R. Martínez-Aguilera, R. Salcedo, M. Castro, Int. J. Quant. Chem. 85 (2001) 546.
[12] A. Edwards, C. Osborne, S. Webster, D. Klenerman, M. Joseph, P. Ostovar, M. Doyle, Corros. Sci. 36 (2) (1994) 315.
[13] V. Jovancicevic, S. Ramachandran, Corrosion 55 (5) (1999) 449.
[14] S. Ramachandran, B.L. Tsai, M. Blanco, H. Chen, Y. Tan, W. Goddard, Langmuir 12 (1996) 6419.
[15] D.A. López, S.N. Simison, S.R. de Sánchez, Electrochim. Acta 48 (2003) 845.
[16] T. Hong, Y.H. Sun, W.P. Jepson, Corros. Sci. 44 (1) (2002) 101.
[17] C.H. Tsai, F. Mansfeld, Corrosion 49 (9) (1993) 726.
[18] K. Bilkova, N. Hackerman, M. Bartos, in: Proceedings of the NACE Corrosion/2002, NACE 2002, Denver, CO, 2002, Paper No. 2284.
[19] C. Liu, Q. Bi, A. Leyland, A. Matthews, Corros. Sci. 45 (5) (2003) 1257.
[20] F.D. de Moraes, J.R. Shadley, J. Chen, E. Rybicki, in: Proceedings of the NACE Corrosion/2000, NACE 2000, Orlando, FL, 2000, Paper No. 30.
[21] G.W. Walter, Corros. Sci. 26 (9) (1986) 681.
[22] Yu.I. Kuztnetsov, Corrosion 89 (1989) I-3-1.
[23] J.L. Crolet, N. Thevenot, A. Dugstad, in: Proceedings of the NACE Corrosion/1999, NACE 1999, San Antonio, TX, 1999, Paper No. 24.
[24] D.A. López, W.H. Schreiner, S.R. de Sánchez, S.N. Simison, The influence of inhibitors molecular structure and steel microstructure on corrosion layers in CO_2 corrosion, An XPS and SEM characterization, Appl. Surf. Sci. (in press).
[25] C.A. Palacios, J.R. Shadley, Corrosion 47 (1991) 122.